

PAPER

Measuring tissue hemodynamics and oxygenation by continuous-wave functional near-infrared spectroscopy—how robust are the different calculation methods against movement artifacts?

To cite this article: Felix Scholkmann *et al* 2014 *Physiol. Meas.* **35** 717

View the [article online](#) for updates and enhancements.

Related content

- [Decoding human mental states by whole-head EEG+fNIRS during category fluency task performance](#)
Ahmet Omurtag, Haleh Aghajani and Hasan Onur Keles
- [Wavelet-based motion artifact removal for functional near-infrared spectroscopy](#)
Behnam Molavi and Guy A Dumont
- [A novel semi-immersive virtual reality visuo-motor task activates ventrolateral prefrontal cortex: a functional near-infrared spectroscopy study](#)
Sara Basso Moro, Marika Carrieri, Danilo Avola *et al*.

Recent citations

- [Applications of Functional Near-Infrared Spectroscopy \(fNIRS\) Neuroimaging in Exercise—Cognition Science: A Systematic, Methodology-Focused Review](#)
Fabian Herold *et al*
- [Movement artefact removal from NIRS signal using multi-channel IMU data](#)
Masudur R. Siddiquee *et al*
- [Functional Near-Infrared Spectroscopy Recordings of Visuospatial Working Memory Processes. Part II: A Replication Study in Children on Sensitivity and Mental-Ability-Induced Differences in Functional Activation](#)
Joëlle Witmer *et al*

Measuring tissue hemodynamics and oxygenation by continuous-wave functional near-infrared spectroscopy—how robust are the different calculation methods against movement artifacts?

Felix Scholkmann¹, Andreas Jaakko Metz^{1,2,3}
and Martin Wolf^{1,4}

¹ Biomedical Optics Research Laboratory, Division of Neonatology,
University Hospital Zurich, 8091 Zurich, Switzerland

² Institute for Biomedical Engineering, ETH Zurich, 8093 Zurich, Switzerland

³ Member of the PhD program imMed, University of Zurich, 8057 Zurich, Switzerland

⁴ Zurich Center for Integrative Human Physiology, University of Zurich, 8057 Zurich,
Switzerland

E-mail: Felix.Scholkmann@usz.ch

Received 13 October 2013, revised 9 January 2014

Accepted for publication 13 February 2014

Published 12 March 2014

Abstract

Continuous-wave near-infrared spectroscopy and imaging enable tissue hemodynamics and oxygenation to be determined non-invasively. Movements of the investigated subject can cause movement artifacts (MAs) in the recorded signals. The strength and type of MAs induced depend on the measurement principle. The aim of the present study was to investigate the quantitative relationship between different single-distance (SD) and multi-distance (MD) measurement methods and their susceptibility to MAs. We found that each method induces MAs to a different degree, and that MD methods are more robust against MAs than SD methods.

Keywords: near-infrared spectroscopy, near-infrared imaging, spatially-resolved, multi-distance, movement artifacts, signal corruption, signal distortion

(Some figures may appear in colour only in the online journal)

1. Introduction

By shining near-infrared (approx. 650–950 nm) light into tissue and measuring the diffuse reflected part from it at different wavelengths in this spectral region, continuous-wave

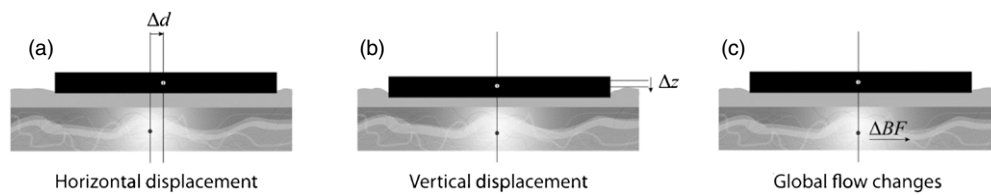


Figure 1. The three main causes of movement artifacts: (a) horizontal displacement (Δd) between the optode and the medium, (b) vertical displacement (Δz), and (c) movement-induced blood flow (ΔBF) changes.

(CW) near-infrared spectroscopy (NIRS) and imaging (NIRI) enable the determination of concentration changes in oxy- and deoxyhemoglobin (O_2Hb , HHb), which reflect changes in tissue hemodynamics and oxygenation (Ferrari and Quaresima 2012, Scholkmann *et al* 2013, Wolf *et al* 2007). When the technique is employed to measure regional changes in hemodynamics and oxygenation of the brain caused by functional tasks (e.g. Biallas *et al* 2012a, 2012b, Holper *et al* 2010, 2012, Wolf *et al* 2002, 2011), the methodology is called functional NIRS (fNIRS) or functional NIRI (fNIRI), depending on the number of source–detector pairs. For ease of reading, we use the term fNIRS for both types of methodology in this paper.

In general there are two types of method to determine the concentrations of O_2Hb ($[O_2Hb]$) and HHb ($[HHb]$) by CW fNIRS. The first type comprises approaches that rely on one single-distance (SD) channel. We name these approaches *single-distance* methods (i.e. SD methods). The second type incorporates approaches relying on several source–detector distances (SDSs) called *multi-distance* methods (i.e. MD methods).

The amount of light detected is dependent on the amount of light coupling into and out of the tissue. Movements of the investigated subject may cause changes in light coupling that generate movement artifacts (MAs) in the optical fNIRS signals. In addition, abrupt blood flow changes due to body movements could be another source of interference resulting in transient changes in the optical signals (Kurihara *et al* 2003). Thus, three main types of effects generate MAs: (i) a horizontal displacement of the fNIRS-optode with respect to the tissue, (ii) a vertical displacement, and (iii) movement-induced changes in blood flow in the tissue investigated (see figure 1). The last type (iii) should be regarded as a specific type—it is not an MA per se since it originates from a physiological effect. However, for the purposes of this paper we also regard this type as an MA since it leads to similar effects as types (i) and (ii). These three types of MAs are not independent and typically occur simultaneously to different extents in real fNIRS measurements. We distinguish the effect of a horizontal or vertical displacement of the NIRS optode relative to the tissue because each movement can cause slightly different effects. For example, the horizontal displacement is often associated with a change in light coupling due to changes of the position of hairs under the optode; whereas the vertical displacement is often associated with a compression of the tissue and thus a change in light coupling and even physiological effects (i.e. squeezing out of blood in the superficial part of the tissue).

Several methods have been developed to remove MAs from the fNIRS signals in offline post-processing (e.g. Barker *et al* 2013, Cooper *et al* 2012, Izzetoglu *et al* 2005, 2010, Molavi and Dumont 2011, Robertson *et al* 2010, Sato *et al* 2006, Scholkmann *et al* 2010). Besides the signal post-processing, the actual type of measurement methods used determines the impact of the MAs on the resulting signals (Yamada *et al* 2009). Although it was stated and observed that MD methods are more robust against MAs compared to SD methods, to the best of our knowledge, no systematic quantitative analysis has been conducted so far to further determine the resilience to MAs.

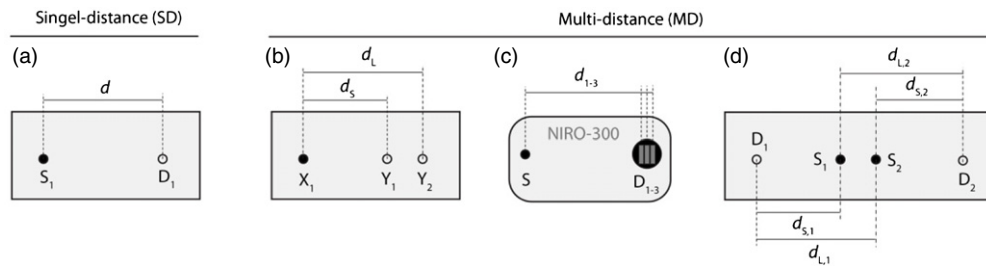


Figure 2. Different SD and MD source–detector geometries. S: source, D: detector, d_S : short distance, d_L : long distance. (a) Classical SD configuration. (b) MD configuration as applied in the ‘spatially-resolved’ technique (MD method 1). Alternatively two sources and one detector can be used, for example. X can either be S or D , and Y either D or S . (c) MD configuration used by the NIRO-300 device (Hamamatsu Photonics, Japan); S : source, D_{1-3} : detectors 1–3 (three-segment photodiode chip, segment length: 2 mm, separation: 1 mm, total length of the chip: 8 mm). (d) MD configuration for the self-calibrating principle (MD method 2). Two short and two long distances are indicated, with the length $d_L = d_{L,1} = d_{L,2}$ and $d_S = d_{S,1} = d_{S,2}$.

Therefore, the aim was to quantify the resilience of different SD and MD methods to induced MAs.

2. Material and methods

2.1. Methods used to determine concentration changes

We investigated six different methods which differ from each other by (i) applying either the SD or MD method, and (ii) by applying different algorithms in order to reduce the influence of changes in hemodynamics and oxygenation in the superficial tissue on the recorded signals. Figure 2 presents the different source–detector arrangements that are required for the various SD and MD methods used in our investigation.

2.1.1. SD method 1: modified Beer–Lambert law. Light transport through tissue is a complex process that can be modeled at a first approximation by the modified Beer–Lambert law (MBLL) (Delpy *et al* 1988, Matcher *et al* 1994):

$$I(\lambda, t) = I_0(\lambda, t) e^{-(\mu_a(\lambda, t) d \text{DPF}(\lambda) + G(\lambda))}, \quad (1)$$

with $I(\lambda, t)$ the measured wavelength-dependent diffuse reflected light intensity, $I_0(\lambda, t)$ the incident light intensity, $\mu_a(\lambda, t)$ the absorption coefficient (cm^{-1}) of the probed tissue, d (cm) the distance between the positions of incident and measured light, i.e. the SDS, $\text{DPF}(\lambda)$ the differential pathlength factor, and $G(\lambda)$ a medium- and geometry-dependent constant. The term $d \text{DPF}(\lambda)$ corresponds to the average light propagation distance in the medium, i.e. the parameter $\text{DPF}(\lambda)$ is a scaling factor that indicates how many times further the detected light has traveled than d . The absorption coefficient in equation (1) can be modeled as

$$\mu_a(\lambda, t) = \sum_{i=0}^n \alpha_i(\lambda) c_i(t) = \frac{1}{\log(e)} \sum_{i=0}^n \varepsilon_i(\lambda) c_i(t), \quad (2)$$

where α_i is the specific molar absorption coefficient ($\text{cm}^{-1} \mu\text{M}^{-1}$), ε_i the specific molar extinction coefficient ($\text{cm}^{-1} \mu\text{M}^{-1}$), and c_i (μM) the concentration of the absorbers i .

Combining equations (1) and (2), and considering two absorbers (O₂Hb, HHb), gives

$$\begin{aligned} A(\lambda, t) &= -\ln\left(\frac{I(\lambda, t)}{I_0(\lambda, t)}\right) = \left(\sum_{i=0}^n \alpha_i(\lambda) c_i(t)\right) d \text{DPF}(\lambda) + G(\lambda) \\ &= (\alpha_{\text{O}_2\text{Hb}}(\lambda) c_{\text{O}_2\text{Hb}}(t) + \alpha_{\text{HHb}}(\lambda) c_{\text{HHb}}(t)) d \text{DPF}(\lambda) + G(\lambda). \end{aligned} \quad (3)$$

Taking the difference between the measurements at two different times (t_0, t_i) cancels the constant $G(\lambda)$. And keeping the incident light intensity constant over time cancels I_0 , too, leading to:

$$\Delta A(\lambda, t) = -\ln\left(\frac{I(\lambda, t)}{I(\lambda, t_0)}\right) = \left(\sum_{i=0}^n \alpha_i(\lambda) \Delta c_i(t)\right) d \text{DPF}(\lambda), \quad (4)$$

with $\Delta c_i(t) = c_i(t) - c_i(t_0)$. To solve equation (4) for the two absorbers ($\Delta c_{\text{O}_2\text{Hb}}(t) = \Delta[\text{O}_2\text{Hb}](t)$, $\Delta c_{\text{HHb}}(t) = \Delta[\text{HHb}](t)$), it is necessary to measure at two wavelengths (λ_1, λ_2). This leads to the following system of equations (Lindkvist *et al* 2013):

$$\begin{bmatrix} \Delta A(\lambda_1, t) \\ \Delta A(\lambda_2, t) \end{bmatrix} = d \begin{bmatrix} \alpha_{\text{HHb}}(\lambda_1) \text{DPF}(\lambda_1) & \alpha_{\text{O}_2\text{Hb}}(\lambda_1) \text{DPF}(\lambda_1) \\ \alpha_{\text{HHb}}(\lambda_2) \text{DPF}(\lambda_2) & \alpha_{\text{O}_2\text{Hb}}(\lambda_2) \text{DPF}(\lambda_2) \end{bmatrix} \begin{bmatrix} \Delta[\text{HHb}](t) \\ \Delta[\text{O}_2\text{Hb}](t) \end{bmatrix}, \quad (5)$$

which than can be solved for the concentration changes given by

$$\begin{bmatrix} \Delta[\text{HHb}](t) \\ \Delta[\text{O}_2\text{Hb}](t) \end{bmatrix} = \frac{1}{d} \begin{bmatrix} \alpha_{\text{HHb}}(\lambda_1) \text{DPF}(\lambda_1) & \alpha_{\text{O}_2\text{Hb}}(\lambda_1) \text{DPF}(\lambda_1) \\ \alpha_{\text{HHb}}(\lambda_2) \text{DPF}(\lambda_2) & \alpha_{\text{O}_2\text{Hb}}(\lambda_2) \text{DPF}(\lambda_2) \end{bmatrix}^{-1} \begin{bmatrix} \Delta A(\lambda_1, t) \\ \Delta A(\lambda_2, t) \end{bmatrix}. \quad (6)$$

When using three or more wavelengths and the specific molar absorption coefficients, the system of equations becomes

$$\begin{bmatrix} \Delta[\text{HHb}](\Delta t) \\ \Delta[\text{O}_2\text{Hb}](\Delta t) \end{bmatrix} = (\mathbf{A}^T \mathbf{A})^{-1} \mathbf{A}^T \begin{bmatrix} \Delta A(\lambda_1, \Delta t) / \text{DPF}(\lambda_1) \\ \vdots \\ \Delta A(\lambda_n, \Delta t) / \text{DPF}(\lambda_n) \end{bmatrix} \frac{1}{d}, \quad (7a)$$

with

$$\mathbf{A} = \begin{bmatrix} \alpha_{\text{HHb}}(\lambda_1) & \alpha_{\text{O}_2\text{Hb}}(\lambda_1) \\ \vdots & \vdots \\ \alpha_{\text{HHb}}(\lambda_n) & \alpha_{\text{O}_2\text{Hb}}(\lambda_n) \end{bmatrix}. \quad (7b)$$

Thus, for each SDS, the absolute *changes* of [O₂Hb] and [HHb] can be calculated. The following values for the specific molar absorption coefficient (given in mm⁻¹ mM⁻¹) were applied in the present study: for O₂Hb: 0.1518 (760 nm), 0.2020 (805 nm), 0.2800 (870 nm), and for HHb: 0.3153 (760 nm), 0.2030 (805 nm), 0.1881 (870 nm). The numerical values of the DPF can be obtained from the literature (e.g. Zhao *et al* 2002), or by using a recently introduced general equation, modeling the DPF as a function of the wavelength and also the age of the investigated subject (Scholkmann and Wolf 2013). For the present study, the DPF was obtained by applying a linear regression to the values for a male adult forehead as published by Duncan *et al* (1995). The resulting DPF values are: 6.11 (760 nm), 5.94 (805 nm), and 5.68 (870 nm). From the $\Delta[\text{O}_2\text{Hb}]$ and $\Delta[\text{HHb}]$ signals, the change in total hemoglobin concentration can be calculated by $\Delta[\text{tHb}] = \Delta[\text{O}_2\text{Hb}] + \Delta[\text{HHb}]$.

2.1.2. SD method 2: modified wavelength-differential Beer–Lambert law with calibration.

A limitation of the MBLL method (as described in section 2.1.1) is that only concentration changes can be determined. Benni *et al* (2005) developed a method to obtain *absolute* concentration values using CW NIRS, based on the groundwork of Hazeki and Tamura (1988), (1989) and Hoshi *et al* (1997).

According to this method, the *absolute* concentrations can be calculated by

$$\begin{bmatrix} [\text{HHb}](t) \\ [\text{O}_2\text{Hb}](t) \end{bmatrix} = \left(\frac{1}{d} \begin{bmatrix} (\alpha_{\text{HHb}}\text{DPF})_{\lambda_1-\lambda_2} & (\alpha_{\text{O}_2\text{Hb}}\text{DPF})_{\lambda_1-\lambda_2} \\ (\alpha_{\text{HHb}}\text{DPF})_{\lambda_3-\lambda_2} & (\alpha_{\text{O}_2\text{Hb}}\text{DPF})_{\lambda_3-\lambda_2} \end{bmatrix} \begin{bmatrix} A_{\lambda_1-\lambda_2}(t) \\ A_{\lambda_3-\lambda_2}(t) \end{bmatrix} - \begin{bmatrix} \Psi_{\text{HHb}} \\ \Psi_{\text{O}_2\text{Hb}} \end{bmatrix} \right), \quad (8a)$$

with

$$A_{\lambda_i-\lambda_j}(t) = -\ln \left(\frac{I(\lambda_i, t) I_0(\lambda_j, t)}{I_0(\lambda_i, t) I(\lambda_j, t)} \right), \quad (8b)$$

and $(\alpha_k\text{DPF})_{\lambda_1-\lambda_2} = \alpha_k\text{DPF}(\lambda_i) - \alpha_k\text{DPF}(\lambda_j) \mid k = \text{HHb}, \text{O}_2\text{Hb}$, as well as the calibration coefficients Ψ_{HHb} and $\Psi_{\text{O}_2\text{Hb}}$ which are determined by a nonlinear regression against reference values obtained from blood. Since we were not able to calibrate against reference blood values, we averaged over the last minute of the measurement and assumed a StO_2 value of 60% as well as a $[\text{O}_2\text{Hb}]$ value of 100 μM . We solved the equation thus

$$\frac{[\text{O}_2\text{Hb}] + \Psi_{\text{O}_2\text{Hb}}}{[\text{O}_2\text{Hb}] + \Psi_{\text{O}_2\text{Hb}} + [\text{HHb}] + \Psi_{\text{HHb}}} = 0.6, \quad (9)$$

and

$$[\text{O}_2\text{Hb}] + \Psi_{\text{O}_2\text{Hb}} = 100 \mu\text{M}. \quad (10)$$

Equation (8) is applied, for example, in the NIRS devices of CASMED (Branford, CT, USA).

The advantage of equation (8) is that absolute values for $[\text{O}_2\text{Hb}]$ and $[\text{HHb}]$ can be obtained. If these are not of interest, the system of equations from Hazeki and Tamura (1988), 1989) and Hoshi *et al* (1997), which do not incorporate a calibration, can be used:

$$\begin{bmatrix} \Delta[\text{HHb}](t) \\ \Delta[\text{O}_2\text{Hb}](t) \end{bmatrix} = \left(\frac{1}{d} \begin{bmatrix} (\alpha_{\text{HHb}}\text{DPF})_{\lambda_1-\lambda_2} & (\alpha_{\text{O}_2\text{Hb}}\text{DPF})_{\lambda_1-\lambda_2} \\ (\alpha_{\text{HHb}}\text{DPF})_{\lambda_3-\lambda_2} & (\alpha_{\text{O}_2\text{Hb}}\text{DPF})_{\lambda_3-\lambda_2} \end{bmatrix}^{-1} \begin{bmatrix} \Delta A_{\lambda_1-\lambda_2}(t) \\ \Delta A_{\lambda_3-\lambda_2}(t) \end{bmatrix} \right), \quad (11)$$

where the Δ indicates time-differential variables as in equation (6). To distinguish equation (10) from (11) in the further course of the paper, the former is referred to *SD method 2a* and the latter to *SD method 2b*.

2.1.3. SD method 3: correlation-based signal improvement. Based on the assumptions that (i) under ideal conditions the changes of $[\text{O}_2\text{Hb}]$ and $[\text{HHb}]$ should be maximally negatively correlated for neuronal activation, and that (ii) changes in the light coupling weaken the negative correlation, Cui *et al* (2010) derived the ‘correlation-based signal improvement’ (CBSI) method to calculate a corrected O_2Hb signal

$$x' = -\frac{1}{2\alpha} (x - \alpha y), \quad (12a)$$

and a corrected HHb signal

$$y' = -\frac{1}{\alpha} x', \quad (12b)$$

with $x = [\text{O}_2\text{Hb}]$ (or $\Delta[\text{O}_2\text{Hb}]$), $y = [\text{HHb}]$ (or $\Delta[\text{HHb}]$), and $\alpha = \sigma(x)/\sigma(y)$, i.e. the ratio of the standard deviations $\sigma(x)$ and $\sigma(y)$. The calculated signals x' and y' are a linear combination of the O_2Hb and HHb signal, and should be more robust against MAs compared to the raw signals. x' is the corrected O_2Hb and y' the corrected HHb signal. Since in principle CBSI can be applied to any O_2Hb and HHb signals, regardless of how it was calculated, we examined how this method influences the signal quality when applied to the other SD methods (1–2) and MD methods (1–3). Thus, this SD method 3 does not offers an algorithm to calculate the hemodynamic/oxygenation signals from the measured raw intensity values, but it is an approach how to increase the resilience of the signals to MA in a signal post-processing step.

2.1.4. MD method1: spatially resolved spectroscopy. A more fundamental description of the light transport through tissue than the MBL is the radiation transfer equation (Haskell *et al* 1994, Lindkvist *et al* 2013)

$$\frac{1}{c} \frac{\partial U(\mathbf{r}, \hat{s}, t)}{\partial t} = -\nabla U(\mathbf{r}, \hat{s}, t) \cdot \hat{s} - (\mu_s + \mu_a) U(\mathbf{r}, \hat{s}, t) + \mu_s + Q(\mathbf{r}, \hat{s}, t), \quad (13)$$

with $U(\mathbf{r}, \hat{s}, t)$ ($\text{W m}^{-2} \text{sr}^{-1}$) the average intensity, c the speed of light, \hat{s} the unit vector pointing in the direction of interest, μ_s the scattering coefficient, \mathbf{r} the position in the three-dimensional space, $P(\hat{s}', \hat{s})$ the normalized differential scatter cross section, and $Q(\mathbf{r}, \hat{s}, t)$ the source term. When $\mu_s' \gg \mu_a$ (μ_s' : reduced scattering coefficient) holds for the medium, by expanding U in spherical harmonics and keeping only the first two terms of the expansion, equation (13) can be simplified to the diffusion equation

$$\frac{1}{c} \frac{\partial \phi(\mathbf{r}, t)}{\partial t} = +\nabla [D \nabla \phi(\mathbf{r}, t)] - \mu_a \phi(\mathbf{r}, t) + Q(\mathbf{r}, t), \quad (14)$$

with $\phi(\mathbf{r}, t)$ the photon fluence rate (W m^{-2}), and D the diffusion coefficient given as $D = 1/3(\mu_a + \mu_s')$. When the diffusion coefficient is spatially invariant, equation (14) results in

$$\frac{1}{c} \frac{\partial \phi(\mathbf{r}, t)}{\partial t} = +D \nabla^2 \phi(\mathbf{r}, t) - \mu_a \phi(\mathbf{r}, t) + Q(\mathbf{r}, t). \quad (15)$$

Employing equation (15), assuming a semi-infinite medium and a point light source emitting a very short pulse and integrating it over time, it is possible to derive an equation relating the attenuation A to the SDS d for the CW case, yielding (Matcher *et al* 1995, Patterson *et al* 1989, Suzuki *et al* 1999)

$$\frac{\partial A(\lambda, t)}{\partial d} = \frac{1}{\ln(10)} \left(\sqrt{3\mu_a(\lambda, t)\mu_s'(\lambda)} + \frac{2}{d} \right), \quad (16)$$

where $A(\lambda, t) = -\log(R(d, \lambda, t))$, with R the reflectance measured at the detector (Suzuki *et al* 1999). The reflectance is defined as the absolute total photon flux density and related to the photon fluence rate by Fick's law (Patterson *et al* 1989) and can be expressed as (under the assumptions $1/\mu_s' \ll d$ and $\mu_a \ll \mu_s'$)

$$R(d, \lambda, t) = \frac{\sqrt{3\mu_a(\lambda, t)\mu_s'(\lambda)}}{2\pi d^2 \mu_s'(\lambda)} e^{-d\sqrt{3\mu_a(\lambda, t)\mu_s'(\lambda)}}. \quad (17)$$

When modeling μ_s' as depending weakly on the wavelength, $\mu_s' = k(1 - h\lambda)$, equation (16) can be solved for the absorption coefficient, giving

$$k\mu_a(\lambda, t) = \frac{1}{3(1 - h\lambda)} \left(\ln(10) \frac{\partial A(\lambda, t)}{\partial d} - \frac{2}{d} \right)^2, \quad (18)$$

with the constants k and h . While k is unknown, h is set, for example, to $6.3 \times 10^{-4} \text{ nm}^{-1}$ in the NIRO-300 device (Hamamatsu Photonics, Japan) (Suzuki *et al* 1999).

The OxyPrem sensor (see section 2.2) in the present study employs shorter SDS than the NIRO-300 device and thus violates the principle that the detectors measuring the absorbance slope are close together with respect to the distance from the source. Therefore we calculated the absorption as

$$k\mu_a(\lambda, t) = \frac{1}{3\mu_s'(\lambda)} \left(\ln(10) \frac{\partial A(\lambda, t)}{\partial d} - 2 \frac{\ln(d_L/d_S)}{d_L - d_S} \right)^2. \quad (19)$$

The values for μ_s' are taken from the literature (Matcher *et al* 1997). This equation can be derived when instead of differentiating $A(d)$ with respect to d , evaluating $\partial A(\lambda)/\partial d = (A(d_L) - A(d_S))/(d_L - d_S)$. This also reveals why the NIRO system needs to have separations between the detectors (δ) much smaller than the SDS. The second terms in equations (18)

and (19) will only become equal when $d_L = d_S + \delta$ and $\delta \ll d_S$. For the calculation of $\partial A / \partial d$ at least two light-paths using one source and two detectors are necessary. Note that when equation (19) is expanded to use two sources and two detectors (similarly to Hueber *et al* (1999)), this calculation of the absorption coefficient yields the same equation as used in the self-calibrating approach (equation (24)).

When measuring $k\mu_a(\lambda)$ for two specific wavelengths (λ_1, λ_2), related to the optical properties of hemoglobin, the following system of equations can be obtained:

$$\begin{bmatrix} k\mu_a(\lambda_1, t) \\ k\mu_a(\lambda_2, t) \end{bmatrix} = \ln(10) \begin{bmatrix} \alpha_{\text{HHb}}(\lambda_1) & \alpha_{\text{O}_2\text{Hb}}(\lambda_1) \\ \alpha_{\text{HHb}}(\lambda_2) & \alpha_{\text{O}_2\text{Hb}}(\lambda_2) \end{bmatrix} \begin{bmatrix} k[\text{HHb}](t) \\ k[\text{O}_2\text{Hb}](t) \end{bmatrix}, \quad (20)$$

with the solution

$$\begin{bmatrix} k[\text{HHb}](t) \\ k[\text{O}_2\text{Hb}](t) \end{bmatrix} = \frac{1}{\ln(10)} \begin{bmatrix} \alpha_{\text{HHb}}(\lambda_1) & \alpha_{\text{O}_2\text{Hb}}(\lambda_1) \\ \alpha_{\text{HHb}}(\lambda_2) & \alpha_{\text{O}_2\text{Hb}}(\lambda_2) \end{bmatrix}^{-1} \begin{bmatrix} k\mu_a(\lambda_1, t) \\ k\mu_a(\lambda_2, t) \end{bmatrix}. \quad (21)$$

Note that the NIRO system calculates these via the MBLL. However, for the present analysis, $[\text{O}_2\text{Hb}]$ and $[\text{HHb}]$ are calculated by equation (21). The NIRO implements this approach to calculate StO_2 (Hamamatsu calls it ‘tissue oxygenation index’, TOI), which is an absolute value, because the unknown factor k cancels out:

$$\text{StO}_2(t) = \frac{k[\text{O}_2\text{Hb}](t)}{k([\text{O}_2\text{Hb}](t) + [\text{HHb}](t))} = \frac{[\text{O}_2\text{Hb}](t)}{([\text{O}_2\text{Hb}](t) + [\text{HHb}](t))}. \quad (22)$$

It should be also pointed out, that the value of StO_2 depends on the wavelength dependence of μ'_s . It has been shown that the wavelength dependence of μ'_s is similar between subjects for the same tissue (Matcher *et al* 1995).

The main advantages of this MD method (called ‘spatially-resolved spectroscopy’, SRS), compared to the traditional SD method is that (i) absolute concentrations can be calculated, and that (ii) this method is less sensitive to hemodynamic and oxygenation changes in the superficial part of the tissue (Al-Rawi *et al* 2001). It is also assumed that this method is less affected by changes in the light coupling, i.e. it is more resilient to MAs. To compare this approach to the others, we calculated $[\text{O}_2\text{Hb}]$, $[\text{HHb}]$ and StO_2 from equation (22).

2.1.5. MD method 2: self-calibrating approach. In 1999, Hueber *et al* (1999) presented a further development of the SRS approach. For this method, at least two detectors (D_1 and D_2) and two sources (S_1 and S_2) are necessary (figure 2(c)). Four detector source combinations result and these should be arranged in such a way that only two different SDSs (a longer, d_L , and a shorter one, d_S) exist, i.e. the distance from source S_1 to detector D_1 (d_{S1}) should be the same as the distance from source S_2 to detector D_2 (d_{S2}). Accordingly, the distance from source S_1 to detector D_2 (d_{L2}) should be the same as the distance from source S_2 to detector D_1 (d_{L1}). The slope (Sl) of the attenuation decrease depending on distance is calculated as

$$Sl(\lambda, t) = \frac{\ln\left(\frac{R(d_{L1}, \lambda, t) R(d_{L2}, \lambda, t)}{R(d_{S1}, \lambda, t) R(d_{S2}, \lambda, t)}\right) + 2 \ln\left(\frac{d_L}{d_S}\right)}{d_L - d_S}. \quad (23)$$

Then μ_a is given as

$$\mu_a(\lambda, t) = Sl(\lambda, t)^2 D(\lambda, t), \quad (24)$$

where the diffusion constant D equals (Metz *et al* 2013):

$$D(\lambda, t) = \frac{1}{3(\mu_a(\lambda, t) + \mu'_s(\lambda))} \cong \frac{1}{3\mu'_s(\lambda)}. \quad (25)$$

The reflectance R in equation (23) may be substituted with the detected intensity. This approach cancels out light tissue coupling, superficial inhomogeneity and detector sensitivity as long as the coupling from one source affects both detectors in the same way and vice versa, and providing there is no light short circuiting along the surface of the tissue.

It should be noted that the original method presented by Hueber *et al* (1999) was designed for frequency domain fNIRS, enabling the direct measurement of μ'_s . In the case of the CW methodology, μ'_s has to be obtained from literature.

2.1.6. MD method 3: modified Beer–Lambert law with short channel regression. Fabbri *et al* (2004) showed that the influence of the superficial component of the probed tissue can be removed by simply performing measurements with two SDS (short and long) and using the equation

$$\Delta A_c(\lambda, t) = \Delta A_L(\lambda, t) - \alpha \Delta A_S(\lambda, t), \quad (26)$$

with $\Delta A_c(\lambda, t)$ the corrected attenuation, $\Delta A_L(\lambda, t)$ the attenuation of the long SDS (sampling brain and superficial components), and $\Delta A_S(\lambda, t)$ corresponding to the short one (sampling superficial components only). According to Fabbri *et al* (2004) the parameter α can be determined by calculating the ratio $\Delta A_L(\lambda, t)/\Delta A_S(\lambda, t)$ during a time interval when μ_a is constant in the cerebral layer—a requirement that is only valid for special conditions. To circumvent this drawback, Saager and Berger (2005) showed that the parameter α can be calculated directly using a least-squares approach:

$$\alpha = \frac{\Delta A_S(\lambda, t) \circ \Delta A_L(\lambda, t)}{\Delta A_S(\lambda, t) \circ \Delta A_S(\lambda, t)}, \quad (27)$$

i.e. a quotient of two scalar products. Saager and Berger (2005) showed that when calculating the parameter value for every segment in an experimental block-paradigm, the influence of the superficial layer can be removed properly.

2.2. Experimental protocol

In order to test the extent to which the six different methods are resilient to MAs, we measured the light attenuation during four different experimental tasks using a novel CW NIRS device, the OxyPrem, which is similar to a previously developed wireless spectrophotometer (Muehleman *et al* 2008). The device features two light detectors and four sources at two different SDSs (1.5 and 2.5 cm), and performs measurement at three wavelengths (760, 805 and 870 nm).

The OxyPrem was attached over the left prefrontal cortex of two subjects (age: 29 and 31 years). In general, our experimental paradigm consisted of two phases: rest, and a task (duration: 1–2 s). Between each task, several minutes were waited to enable the signal to reach a stable state again. Four different tasks were performed: (a) fast horizontal movement of the head to the left and right, (b) strong pressing onto the optode with the index finger (i.e. vertical displacement), (c) movement of the head down and up, (d) short frowning. Each of the tasks causes a different kind of MA. In total, four measurements were performed (subject one performed tasks 1–2, subject two tasks 3–4). The tasks were repeated six times each. For a diagram of the experimental tasks please refer to figure 3.

After recording the raw optical data, the $[O_2Hb]$, $[HHb]$ and StO_2 signals were calculated for all six different methods as presented in the previous subsections.

2.3. Performance analysis of the different methods

To quantify the impact of the four types of movement on the calculated signals, (i) for each signal a block average was calculated, starting 10 s before each task (i.e. the induced MA) and ending 10 s after the end of each task; (ii) the block average was divided into three intervals: a pre-task baseline ($t_{pre} = -10, \dots, -8$ s), a task interval (with slightly varying duration

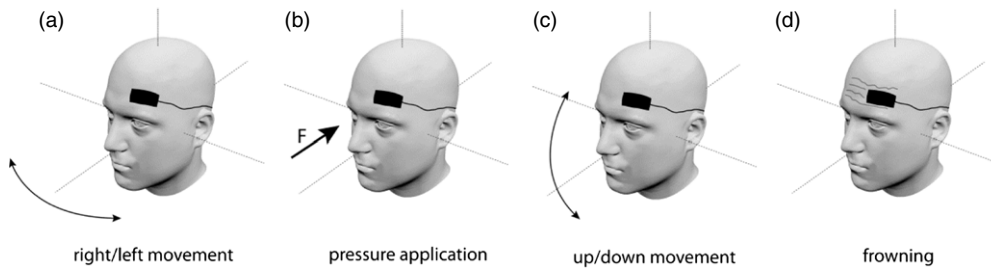


Figure 3. The four tasks to induce movement artifacts.

depending on the actual measurement, in general: $t_{\text{task}} = -1, \dots, 1$ s), and a post-baseline interval ($t_{\text{post}} = 8, \dots, 10$ s); (iii) the parameters q_1 – q_3 were calculated. The first parameter q_1 is defined as

$$q_1 = m_{\text{post}} - m_{\text{pre}}, \quad (28)$$

with m_{post} the median of the post-task baseline, and m_{pre} the median of the pre-task baseline, respectively. This represents a baseline shift caused by the movement. Significant baseline changes are marked by an asterisk above the top right panel in figures 6 and 7. Significance was tested by a paired t -test between m_{post} and m_{pre} . Analogously, q_2 was defined as

$$q_2 = m_{\text{task}} - m_{\text{pre}}, \quad (29)$$

with m_{task} the median of the task-interval. The value of q_2 will be high if the artifact peak is large. The parameter q_3 is given by

$$q_3 = \text{med} \left(\frac{\text{MAD}_{\text{task}}}{\text{MAD}_{\text{pre}}} \right), \quad (30)$$

i.e. the median (med) of the quotient given by the median absolute deviation (MAD) of the task interval divided by the MAD of the pre-task interval. q_3 has a high value in cases where the artifact causes a larger standard deviation in the task period compared to the baseline period and when a large peak artifact is observed. Significant MAD changes are indicated by an asterisk above the middle gray bar in figures 6 and 7. Significance was tested using a paired t -test of $m_{\text{task}}/m_{\text{pre}}$ against 1. False discovery rate correction was performed to account for multiple testing (Benjamini and Hochberg 1995) (104 tests in total).

From these three parameters (q_1 – q_3), a score Q was calculated that quantifies the strength of an MA for a given time series:

$$Q = |q_1| + |q_2| + |q_3|. \quad (31)$$

The parameter Q was derived heuristically by optimizing the best correlation between the parameter values and an expert's decision about the strength of the MA. The higher the value of Q , the stronger the MA.

We accounted for tissue heterogeneities by normalizing the Q values to the number of light-paths. For example the MD method 2 uses four light-paths whereas the SD method 1 only one. Thus, for the same light-paths, for MD method 2 only one Q value could be calculated, but four Q values for SD method 1. These were averaged to achieve a normalization.

In addition, the mean of Q values for all four tasks were averaged for each algorithm. This parameter was denoted as $\langle Q \rangle$.

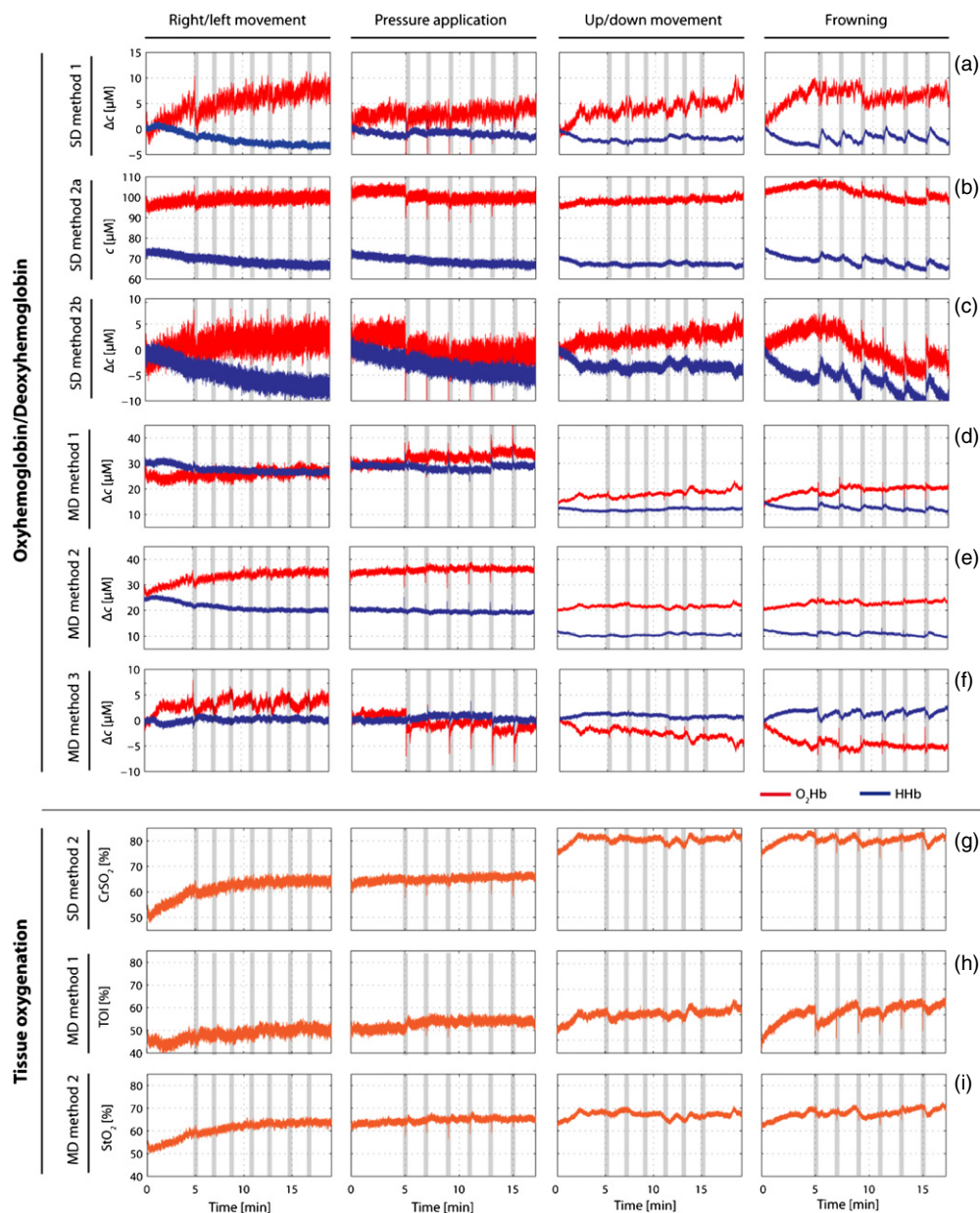


Figure 4. Time courses for all calculated signals and all four tasks. The intervals when the tasks were performed are marked with grey bars. Time courses of concentration of oxyhemoglobin [O_2Hb] are in red and [HHb] in blue. For SD method 2, two rows are presented ((a) and (b)), as explained in the corresponding section in the text. The only difference between the two methods is the absolute values of O_2Hb and HHb , which is 70–100 μM for the (a) case but approximately 0 for the (b) case, the relative time course is the same. Note that time courses were not averaged to represent all the same number light-paths.

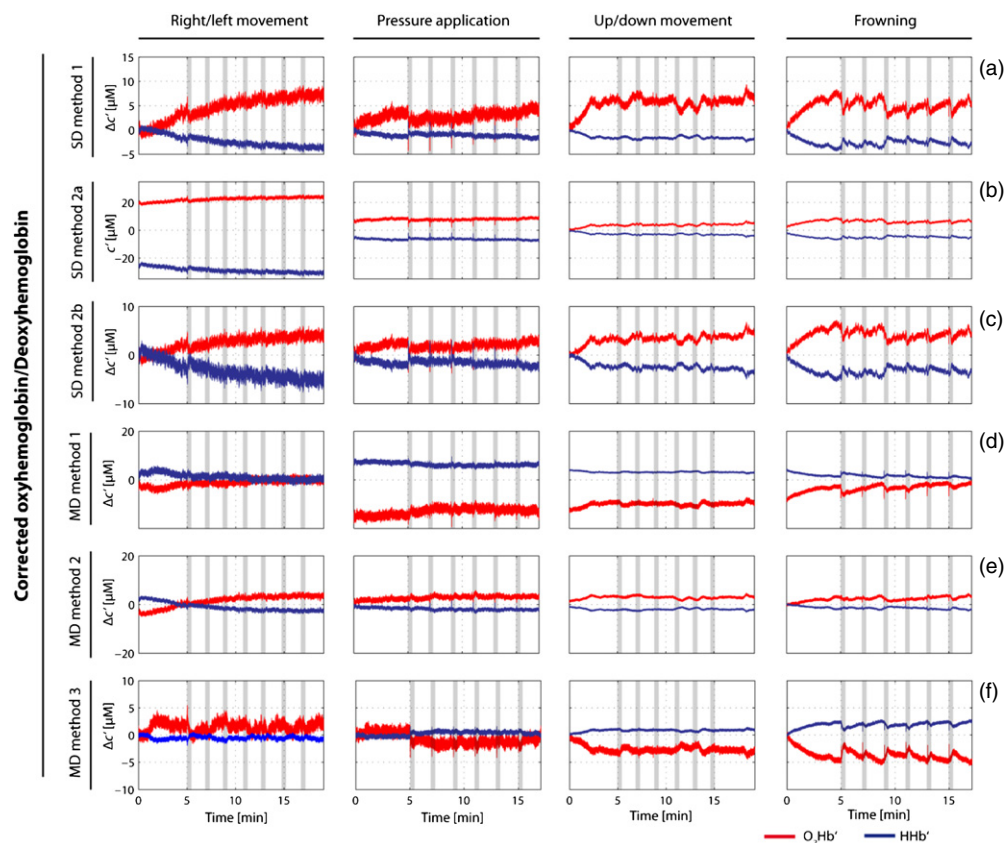


Figure 5. As figure 4, but the correlation based signal improvement (CBSI, SD method 3) was calculated for the $[O_2Hb]$ and $[HHb]$ time series. Note that the scales are similar to figure 4.

3. Results

The temporal evolution of the time series for all four tasks and algorithms is given in figure 4 (SD methods 1–2 and MD methods 1–3) and figure 5 (SD method 3). The block averages of the task-related signal changes are depicted in figures 6 and 7. Table 1 lists the Q values for all tasks and algorithms, and in figure 8 the Q values for each algorithm are displayed.

In general, figures 6 and 7 clearly show (i) that the impact of movements on the calculated signals depends on the algorithm, (ii) that the traditional CW NIRS approach (the MBLL, i.e. SD method 1) performs worst compared to all other algorithms, (iii) that task 2 (pressure application) causes the strongest MAs in O_2Hb , whereas task 4 (frowning) causes the strongest MAs in HHb . $\langle Q \rangle$ was reduced in all methods compared to SD method 1 and the largest reduction (i.e. improvement of signal quality) was found for MD method 2 (49.6% in O_2Hb and 55.3% in HHb).

Concerning the SD methods, the SD method 2 had lower Q values (i.e. is less affected by MAs) for HHb signals compared to SD method 1. For O_2Hb signals the Q values were comparable. The MD methods showed in general lower Q values than the SD methods, and this was particularly clear in O_2Hb calculated using MD method 2. The Q values for the oxygen

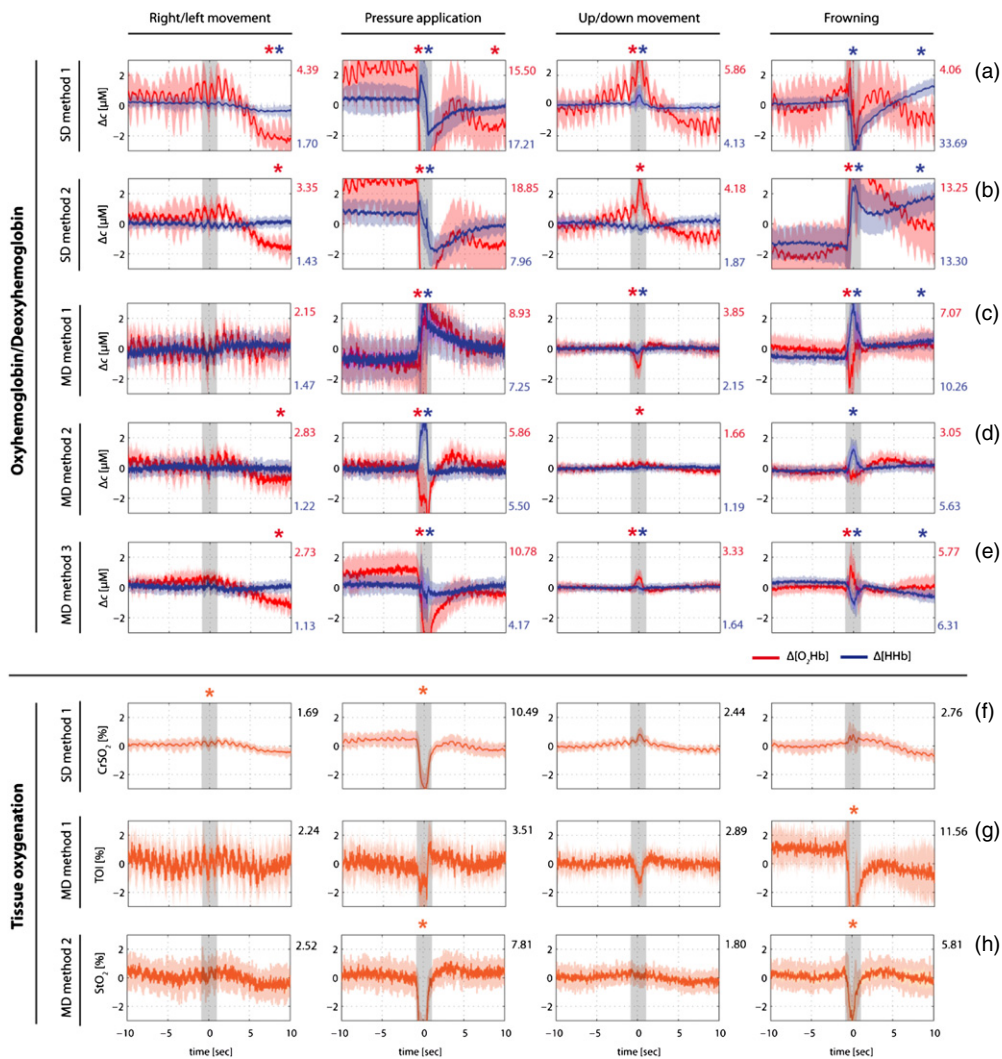


Figure 6. Block averages for all calculated signals and all four tasks. The mean value was subtracted from each block before averaging. Mean time courses are presented and the shaded areas represent the 95% confidence interval. Grey bars in the middle represent task time (i.e. when the artifact was induced). Asterisks above the grey bars indicate a significantly higher MAD of the artifact compared to the MAD of the baseline (criteria q_3 , e.g. seen for all up/down movement, except for row (g)). An asterisks on the top right of the panel indicates a significant baseline shift induced by the artifact (e.g. row (a), first and second column). Numbers on the right of each panel represent the quality index (Q) related to the block average. Red values represent O_2Hb Q indices and blue values HHb Q indices. Rows (f), (g) and (h) represent tissue oxygenation (StO_2) time courses. The StO_2 Q is also given right of the panel. Note that time courses were not averaged to represent all the same number of light-paths. For this reason, the quality indices observed here may not be equal to the quality indices given in table 1.

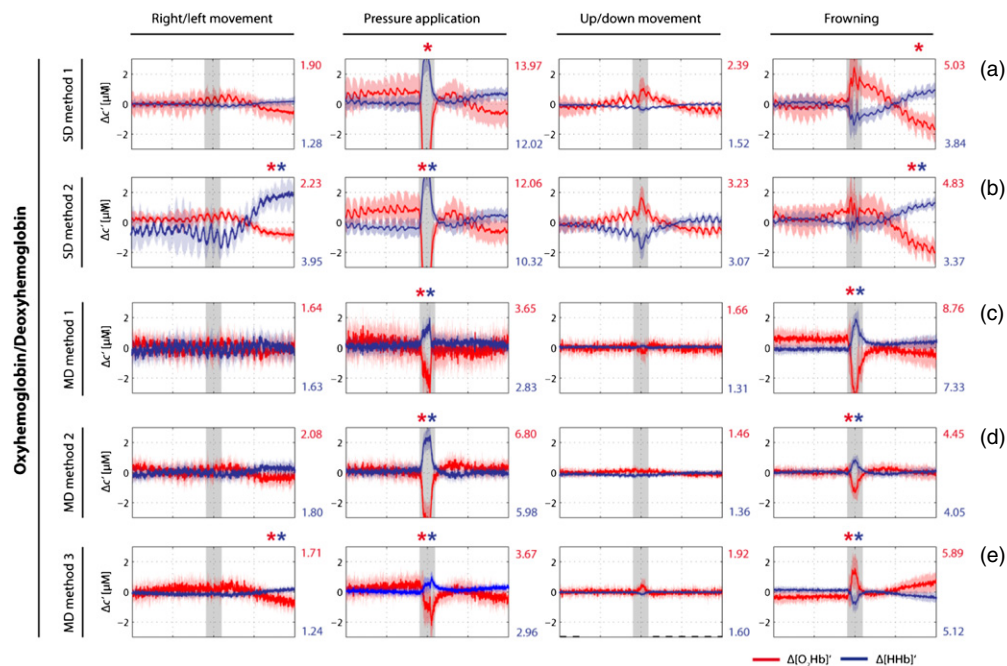


Figure 7. As figure 6, but the correlation based signal improvement (CBSI) method was applied to the signals.

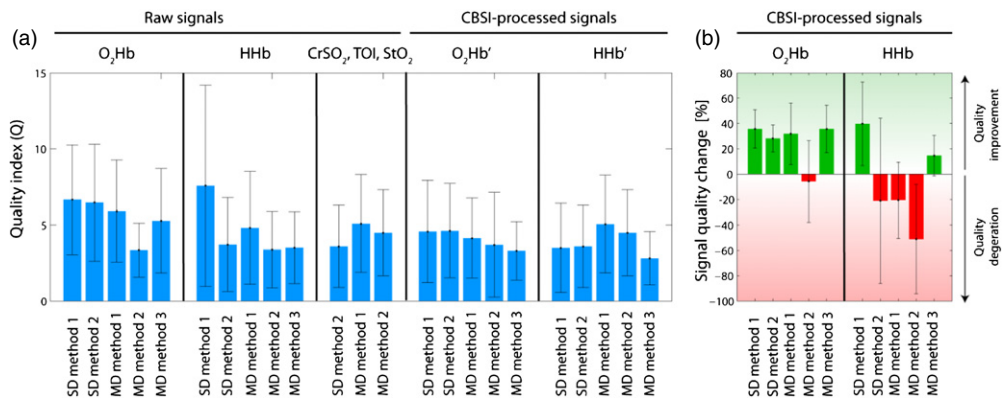


Figure 8. (a) Visualization of table 1. The mean of the Q values for each method and signal. Error bars represent standard deviation. (b) Visualization of table 2, i.e. shown is the improvement of the quality value for each method when applying the CBSI method. O₂Hb: oxyhemoglobin, HHb: deoxyhemoglobin. CrSO₂, TOI, StO₂: The different terms for tissue oxygen saturation related to the method employed to calculate it: cerebral regional oxygen saturation (CrSO₂, SD method 2), tissue oxygen index (TOI, MD method 1), tissue oxygen saturation, respectively (StO₂, MD method 2).

Table 1. For the four tasks, the quality indices for oxygenated and deoxygenated hemoglobin (O₂Hb and HHb, respectively) and tissue oxygenation (StO₂, TOI, CrSO₂) time courses are given. Lower *Q* values indicate better signal quality, i.e. the effect of the MAs is reduced. For O₂Hb and HHb, lowest values are obtained with MD method 2. For StO₂, lowest values are obtained for MD method 3. SD method 1: MBLL (Delpy *et al* 1988). SD method 2: As used in Benni *et al* (2005) and Hazeki and Tamura (1989). MD method 1: SRS, as used in the NIRO system (Matcher *et al* 1995, Suzuki *et al* 1999). MD method 2: As used in Hueber *et al* (1999). MD method 3: As used in Saager and Berger (2005). *Q* values are averaged over the four same light-paths.

<i>Q</i> values O ₂ Hb						
	Right/left movement	Pressure application	Up/down movement	Frowning	Sum	Mean (<i>Q</i>) ± SD
SD method 1	3.58	11.83	4.97	6.21	26.59	6.65 ± 3.61
SD method 2	2.74	11.11	3.94	8.03	25.83	6.46 ± 3.84
MD method 1	3.31	10.60	3.73	5.98	23.62	5.91 ± 3.35
MD method 2	2.83	5.86	1.66	3.05	13.40	3.35 ± 1.78
MD method 3	2.85	10.26	3.22	4.74	21.07	5.27 ± 3.43

<i>Q</i> values HHb						
	Right/left movement	Pressure application	Up/down movement	Frowning	Sum	Mean (<i>Q</i>) ± SD
SD method 1	1.52	9.28	3.32	16.16	30.27	7.57 ± 6.62
SD method 2	1.43	3.86	1.52	8.02	14.82	3.71 ± 3.09
MD method 1	1.38	8.82	1.95	7.08	19.23	4.81 ± 3.71
MD method 2	1.22	5.5	1.19	5.62	13.53	3.38 ± 2.52
MD method 3	1.24	5.83	1.71	5.28	14.05	3.51 ± 2.37

<i>Q</i> values TOI, StO ₂ , CrSO ₂						
	Right/left movement	Pressure application	Up/down movement	Frowning	Sum	Mean (<i>Q</i>) ± SD
SD method 2	1.57	7.52	2.14	3.11	14.35	3.59 ± 2.70
MD method 1	2.18	7.48	2.40	8.18	20.26	5.06 ± 3.21
MD method 2	2.52	7.81	1.80	5.81	17.95	4.49 ± 2.82

Table 2. Improvement of *Q* when applying SD method 3 (Cui *et al* 2010) on the different [O₂Hb] and [HHb] time courses. Change is given in %, relative to the original *Q* value stated in table 1. A positive value indicates a reduced *Q* and therefore a reduction of the artifact in the signal i.e. SD method 3 further improves signal quality; however on the cost of more difficult data interpretation. For abbreviations see caption of table 1.

Change in <i>Q</i> values O ₂ Hb (representative)					
	Right/left movement	Pressure application	Up/down movement	Frowning	Mean
SD method 1	+43.69	+21.58	+53.28	+24.70	+35.81
SD method 2	+23.88	+18.93	+26.45	+43.54	+28.20
MD method 1	+37.58	+37.17	+55.31	− 2.24	+31.95
MD method 2	+26.72	− 16.03	+12.31	− 45.82	− 5.71
MD method 3	+39.03	+46.30	+49.36	+8.40	+35.77

Change in <i>Q</i> values HHb (representative)					
	Right/left movement	Pressure application	Up/down movement	Frowning	Mean
SD method 1	+7.54	+17.55	+55.48	+78.68	+39.81
SD method 2	− 9.68	− 95.14	− 40.34	+61.17	− 21.00
MD method 1	− 57.89	+15.15	− 23.61	− 15.62	− 20.49
MD method 2	− 107.47	− 42.07	− 51.47	− 3.26	− 51.07
MD method 3	− 7.20	+15.58	+18.57	+31.58	+14.63

saturation signals (CrSO_2 , TOI and StO_2) calculated using the SD method 2 and MD methods 1–2 were quite similar.

4. Discussion and conclusion

We aimed to quantify the robustness of different SD and MD methods against MAs. To the best of our knowledge, this is the first systematic analysis with regard to this issue.

Our analysis revealed that (i) the MD methods are superior to the SD methods in terms of resilience to MAs; (ii) the SD method 1 (i.e. the modified Beer–Lambert law (MBLL)) is strongly affected by movements which led to the strongest MAs in the calculated signals compared to all other algorithms employed by our analysis; (iii) artifacts in SD method 1 can be reduced significantly by employing SD method 3 (i.e. correlation-based signal improvement (CBSI)); (iv) SD method 3 applied to MD method 3 (i.e. the MBLL with short channel regression) improves the signal quality, which is not the case for SD method 2 (i.e. the modified wavelength-differential Beer–Lambert law with calibration; implemented in the CASMED devices) or MD methods 1 (i.e. spatially resolved spectroscopy; implemented in the NIRO-300 device) and 2 (i.e. the self-calibrating approach); and most importantly (v) the strength and type of MA in a NIRS signal depend on the algorithms used to calculate the hemodynamic and oxygenation values.

We took care to implement the algorithms as close as possible to the original intended applications stated by the authors. However, the MD method 1 slightly violates our sensor geometry, i.e. the requirements for the source–detector configuration (Suzuki *et al* 1999) are not completely fulfilled. To correct for this issue, we slightly adapted the original algorithm of MD method 1 to two detectors with greater distance to each other (i.e. 1.0 cm) as compared to the original method (<5 mm). Hence, the robustness of the NIRO device may differ from our evaluation of the algorithm. Furthermore, NIRO uses the MBLL to calculate changes in O_2Hb and HHb , but we used equation (19).

Regarding SD method 3 (i.e. CBSI), our analysis showing a reduction in MAs when applying this method is in agreement with the analysis of Cui *et al* (2010) which showed that ‘large spikes visually evident in the original signal are largely removed by the CBSI method’ (Cui *et al* 2010). However, one drawback of this method is that (i) it should be applied only to NIRS signals with task-evoked changes, and (ii) their physiological interpretation is not straight-forward since the method assumes that O_2Hb and HHb were perfectly negatively correlated during a hemodynamic response, which is only partially true for real data.

We also observed that MD methods are more resilient to MAs compared to SD methods. In addition MD methods remove the influence of the superficial tissue (Al-Rawi *et al* 2001, Canova *et al* 2011, Franceschini *et al* 1998), thus they are superior to SD methods and recommended for NIRS applications. This feature is particularly of interest for the detection of task-evoked brain activity (i.e. the hemodynamic response) which is accompanied by changes in hemodynamics in the superficial tissue too (Gagnon *et al* 2012, Kirilina *et al* 2012, 2013, Klaessens *et al* 2004, 2005, Okada and Delpy 2003). Compared to the other MD methods, MD method 3 (i.e. the MBLL with short channel regression) seems to have a slight disadvantage in that sense that the channel with the short SDS (1.5 cm) contains also a small amount of information related to the hemodynamic activity in deeper tissue layers (i.e. the gray matter) which is then regressed out from the channel with the longer SDS (i.e. 2.5 cm). This could reduce slightly the sensitivity to detect evoked hemodynamic changes due to brain activity. A solution is to use a short channel with a SDS of only a few mm.

In addition, it should be noted that the correct quantification of the concentrations by all the SD and MD methods depends on the correct assumption of μ'_s or the DPF.

Our analysis revealed that for specific tasks, e.g. the pressure application, MAs were not completely removed by either algorithm. Therefore, application of specially designed signal processing algorithms will further reduce MAs, e.g. (Barker *et al* 2013, Cooper *et al* 2012, Izzetoglu *et al* 2005, 2010, Molavi and Dumont 2011, Robertson *et al* 2010, Sato *et al* 2006, Scholkmann *et al* 2010).

In summary, we performed a quantitative analysis concerning the effect of MAs on $[O_2Hb]$, $[HHb]$ and StO_2 signals calculated using different methods. To the best of our knowledge, no analysis of this type had previously been performed to date. Our results showed that the MA impact was high when calculating these signals using the MBLL. Signal quality was improved most by applying MD methods (self-calibrating principle, spatially resolved spectroscopy, Saager–Berger approach). The maximum signal quality increase was observed for MD method 2 (i.e. the self-calibrating MD approach).

References

- Al-Rawi P G, Smielewski P and Kirkpatrick P J 2001 Evaluation of a near-infrared spectrometer (NIRO-300) for the detection of intracranial oxygenation changes in the adult head *Stroke* **32** 2492–500
- Barker J W, Aarabi A and Huppert T J 2013 Autoregressive model based algorithm for correcting motion and serially correlated errors in fNIRS *Biomed. Opt. Express* **4** 1366–79
- Benjamini Y and Hochberg Y 1995 Controlling the false discovery rate: a practical and powerful approach to multiple testing *J. R. Stat. Soc. B* **57** 289–300
- Benni P B *et al* 2005 Validation of the Cas Neonatal NIRS system by Monitoring VV-ECMO Patients *Adv. Exp. Med. Biol.* **566** 195–201
- Biallas M *et al* 2012a How to conduct studies with neonates combining near-infrared imaging and electroencephalography *Adv. Exp. Biol. Med.* **737** 111–7
- Biallas M *et al* 2012b Multimodal recording of brain activity in term newborns during photic stimulation by near-infrared spectroscopy and electroencephalography *J. Biomed. Opt.* **17** 086011
- Canova D *et al* 2011 Inconsistent detection of changes in cerebral blood volume by near infrared spectroscopy in standard clinical tests *J. Appl. Physiol.* **110** 1646–55
- Cooper R J *et al* 2012 A systematic comparison of motion artifact correction techniques for functional near-infrared spectroscopy *Front. Neurosci.* **6** 147
- Cui X, Bray S and Reiss A L 2010 Functional near infrared spectroscopy (NIRS) signal improvement based on negative correlation between oxygenated and deoxygenated hemoglobin dynamics *Neuroimage* **49** 3039–46
- Delpy D T *et al* 1988 Estimation of optical pathlength through tissue from direct time of flight measurement *Phys. Med. Biol.* **33** 1433–42
- Duncan A *et al* 1995 Optical pathlength measurements on adult head, calf and forearm and the head of the newborn infant using phase resolved optical spectroscopy *Phys. Med. Biol.* **40** 295–304
- Fabbri F *et al* 2004 Optical measurements of absorption changes in two-layered diffusive media *Phys. Med. Biol.* **49** 1183–201
- Ferrari M and Quaresima V 2012 A brief review on the history of human functional near-infrared spectroscopy (fNIRS) development and fields of application *Neuroimage* **63** 921–35
- Franceschini M A *et al* 1998 Influence of a superficial layer in the quantitative spectroscopic study of strongly scattering media *Appl. Opt.* **37** 7447–58
- Gagnon L *et al* 2012 Quantification of the cortical contribution to the NIRS signal over the motor cortex using concurrent NIRS-fMRI measurements *Neuroimage* **59** 3933–40
- Haskell R C *et al* 1994 Boundary conditions for the diffusion equation in radiative transfer *J. Opt. Soc. Am. A* **11** 2727–40
- Hazeki O and Tamura M 1988 Quantitative analysis of hemoglobin oxygenation state of rat brain *in situ* by near-infrared spectrophotometry *J. Appl. Physiol.* **64** 796–802
- Hazeki O and Tamura M 1989 Near infrared quadruple wavelength spectrophotometry of the rat head *Adv. Exp. Med. Biol.* **248** 63–69
- Holper L *et al* 2010 Testing the potential of a virtual reality neurorehabilitation system during performance of observation, imagery and imitation of motor actions recorded by wireless functional near-infrared spectroscopy (fNIRS) *J. Neuroeng. Rehabil.* **7** 57

- Holper L *et al* 2012 Extension of mental preparation positively affects motor imagery: a functional near-infrared spectroscopy study *Cortex* **48** 593–603
- Hoshi Y *et al* 1997 Redox behavior of cytochrome oxidase in the rat brain measured by near-infrared spectroscopy *J. Appl. Physiol.* **83** 1842–8
- Hueber D *et al* 1999 New optical probe designs for absolute (self-calibrating) NIR tissue hemoglobin measurements *Proc. SPIE* **3597** 618–30
- Izzetoglu M *et al* 2005 Motion artifact cancellation in NIR spectroscopy using Wiener filtering *IEEE Trans. Biomed. Eng.* **52** 934–8
- Izzetoglu M *et al* 2010 Motion artifact cancellation in NIR spectroscopy using discrete Kalman filtering *Biomed. Eng. Online* **9** 16
- Kirilina E *et al* 2012 The physiological origin of task-evoked systemic artefacts in functional near infrared spectroscopy *Neuroimage* **61** 70–81
- Kirilina E *et al* 2013 Identifying and quantifying main components of physiological noise in functional near infrared spectroscopy on the prefrontal cortex *Front. Hum. Neurosci.* **7** 864
- Klaessens J H G M *et al* 2004 *In vivo* measurements of the influence of the skin on cerebral oxygenation changes measured with near-infrared spectrophotometry (NIRS) *Proc. SPIE* **5318** 85–93
- Klaessens J H G M *et al* 2005 Effects of skin on bias and reproducibility of near-infrared spectroscopy measurement of cerebral oxygenation changes in porcine brain *J. Biomed. Opt.* **10** 044003
- Kurihara K, Kikukawa A and Kobayashi A 2003 Cerebral oxygenation monitor during head-up and -down tilt using near-infrared spatially resolved spectroscopy *Clin. Physiol. Funct. Imaging* **23** 177–81
- Lindkvist M, Granåsen G and Grönlund C 2013 Coherent derivation of equations for differential spectroscopy and spatially resolved spectroscopy: an undergraduate tutorial *Spectrosc. Lett.* **46** 243–9
- Matcher S J, Cope M and Delpy D T 1994 Use of the water absorption spectrum to quantify tissue chromophore concentration changes in near-infrared spectroscopy *Phys. Med. Biol.* **39** 177–96
- Matcher S J, Cope M and Delpy D T 1997 *In vivo* measurements of the wavelength dependence of tissue-scattering coefficients between 760 and 900 nm measured with time-resolved spectroscopy *Appl. Opt.* **36** 386–96
- Matcher S J *et al* 1995 Absolute quantification methods in tissue near-infrared spectroscopy *Proc. SPIE* **2359** 486–95
- Metz A *et al* 2013 The effect of basic assumptions on the tissue oxygen saturation value of near infrared spectroscopy *Adv. Exp. Med. Biol.* **765** 169–75
- Molavi B and Dumont G A 2011 Wavelet-based motion artifact removal for functional near-infrared spectroscopy *Physiol. Meas.* **33** 259–70
- Muehleemann T, Haense D and Wolf M 2008 Wireless miniaturized *in-vivo* near infrared imaging *Opt. Exp.* **16** 10323–30
- Okada E and Delpy D T 2003 Near-infrared light propagation in an adult head model. II. Effect of superficial tissue thickness on the sensitivity of the near-infrared spectroscopy signal *Appl. Opt.* **42** 2915–22
- Patterson M S, Schwarz E and Wilson B C 1989 Quantitative reflectance spectrophotometry for the non-invasive measurement of photosensitizer concentrations in tissue during photodynamic therapy *Proc. SPIE* **1065** 115–22
- Robertson F C, Douglas T S and Meintjes E M 2010 Motion artifact removal for functional near infrared spectroscopy: a comparison of methods *IEEE Trans. Biomed. Eng.* **57** 1377–87
- Saager R B and Berger A J 2005 Direct characterization and removal of interfering absorption trends in two-layer turbid media *J. Opt. Soc. Am. A* **22** 1874–82
- Sato H *et al* 2006 Wavelet analysis for detecting body-movement artifacts in optical topography signals *Neuroimage* **33** 580–7
- Scholkmann F and Wolf M 2013 General equation for the differential pathlength factor of the frontal human head depending on wavelength and age *J. Biomed. Opt.* **18** 105004
- Scholkmann F *et al* 2010 How to detect and reduce movement artifacts in near-infrared imaging using moving standard deviation and spline interpolation *Physiol. Meas.* **31** 649–62
- Scholkmann F *et al* 2013 A review on continuous wave functional near-infrared spectroscopy and imaging instrumentation and methodology *Neuroimage* **85** 6–27
- Suzuki S *et al* 1999 A tissue oxygenation monitor using NIR spatially resolved spectroscopy *Proc. SPIE* **3597** 582–92
- Wolf M, Ferrari M and Quaresima V 2007 Progress of near-infrared spectroscopy and topography for brain and muscle clinical applications *J. Biomed. Opt.* **12** 062104

- Wolf M *et al* 2002 Different time evolution of oxyhemoglobin and deoxyhemoglobin concentration changes in the visual and motor cortices during functional stimulation: a near-infrared spectroscopy study *Neuroimage* **16** 704–12
- Wolf U *et al* 2011 Changes in hemodynamics and tissue oxygenation saturation in the brain and skeletal muscle induced by speech therapy—a near-infrared spectroscopy study *ScientificWorldJournal* **11** 1206–15
- Yamada T, Umeyama S and Matsuda K 2009 Multidistance probe arrangement to eliminate artifacts in functional near-infrared spectroscopy *J. Biomed. Opt.* **14** 064034
- Zhao H *et al* 2002 Maps of optical differential pathlength factor of human adult forehead, somatosensory motor and occipital regions at multi-wavelengths in NIR *Phys. Med. Biol.* **47** 2075–93